Downscaled Projections of Extreme Rainfall in New York State

Technical Document

Arthur T. DeGaetano
Christopher M. Castellano

Northeast Regional Climate Center
Cornell University
Ithaca, NY

Table of Contents

Introduction

Background

Extreme precipitation has important implications for urban and rural development, public infrastructure, watershed management, agriculture, and human health. According to the National Weather Service (NWS) Hydrologic Information Center, non-storm surge flooding causes an estimated $7.96 billion in damage (adjusted to 2014 inflation) and 82 fatalities each year in the United States alone. Historical climate records indicate that the northeastern U.S. has experienced significant increases in extreme precipitation since the mid-to-late twentieth century. Upward trends in both the frequency and magnitude of extreme precipitation have been documented by numerous studies (Kunkel et al. 1999; Kunkel 2003; DeGaetano 2009; Karl et al. 2009; Heineman 2012; Kunkel et al. 2013). Moreover, the most recent assessment report from the Intergovernmental Panel on Climate Change (IPCC 2014) suggests that the frequency and magnitude of extreme precipitation in this region are expected to continue to increase throughout the twenty-first century. Such changes will likely exacerbate the societal impacts of extreme precipitation in the future.

Objectives

In consideration of the issues highlighted above, the Northeast Regional Climate Center (NRCC) has partnered with the New York State Energy Research and Development Authority (NYSERDA) to compare various methods of downscaling global climate model (GCM) output and create extreme precipitation projections for New York State. These projections will ultimately be incorporated into climate change adaptation planning. Primary objectives of this research include: 1) evaluation of downscaling method–climate model combinations to assess their ability to replicate historical precipitation extremes, 2) downscaling of projected precipitation extremes for future periods, 3) quantification of methodological and climate model uncertainties, and 4) outreach and development of web-based tools to make results accessible to potential users. Final project deliverables include:

1) Historical and future 2-, 5-, 10-, 25-, 50-, and 100-year recurrence interval precipitation amounts computed for 1-, 2-, 3-, 6-, 12-, 18-, and 24-hour durations
2) Historical and future intensity-duration-frequency (IDF) curves
3) An interactive webpage allowing the public to navigate final research products

Data

Observational Data

The geographical domain for this study consists of 157 NWS Cooperative Observer Program (COOP) stations with long-term daily precipitation data in New York and portions of adjacent states and Canada (Figure 1). To qualify as long-term, a given station must meet one of the following criteria: 1) reported valid precipitation observations for at least 95% of all days during the 1961–2010 period, 2) reported valid precipitation observations for at least 85% of all days during the 1961–2010 period and is located at least 25 km from the nearest 95% station, or

3) reported valid precipitation observations for at least 75% of all days during the 1961–2010 period and is located at least 25 km from the nearest 85% and 95% stations. The last two criteria were necessary to achieve adequate station density. Daily precipitation data at each station were obtained from the Applied Climate Information System (ACIS), which is maintained by the National Oceanic and Atmospheric Administration (NOAA) Regional Climate Centers (RCCs). The primary source of daily climate data for the ACIS database is the Global Historical Climatology Network (GHCN). A table containing each station's COOP ID, name, state, latitude, longitude, and elevation is provided in Appendix A. In addition to daily precipitation data, this study uses 6-hourly gridded atmospheric data from National Centers for Environmental Prediction–National Center for Atmospheric Research (NCEP–NCAR) reanalysis (Kalnay et al. 1996). The NCEP–NCAR reanalysis data is available at 2.5° × 2.5° horizontal resolution and 17 vertical pressure levels between 1000-hPa and 10-hPa.

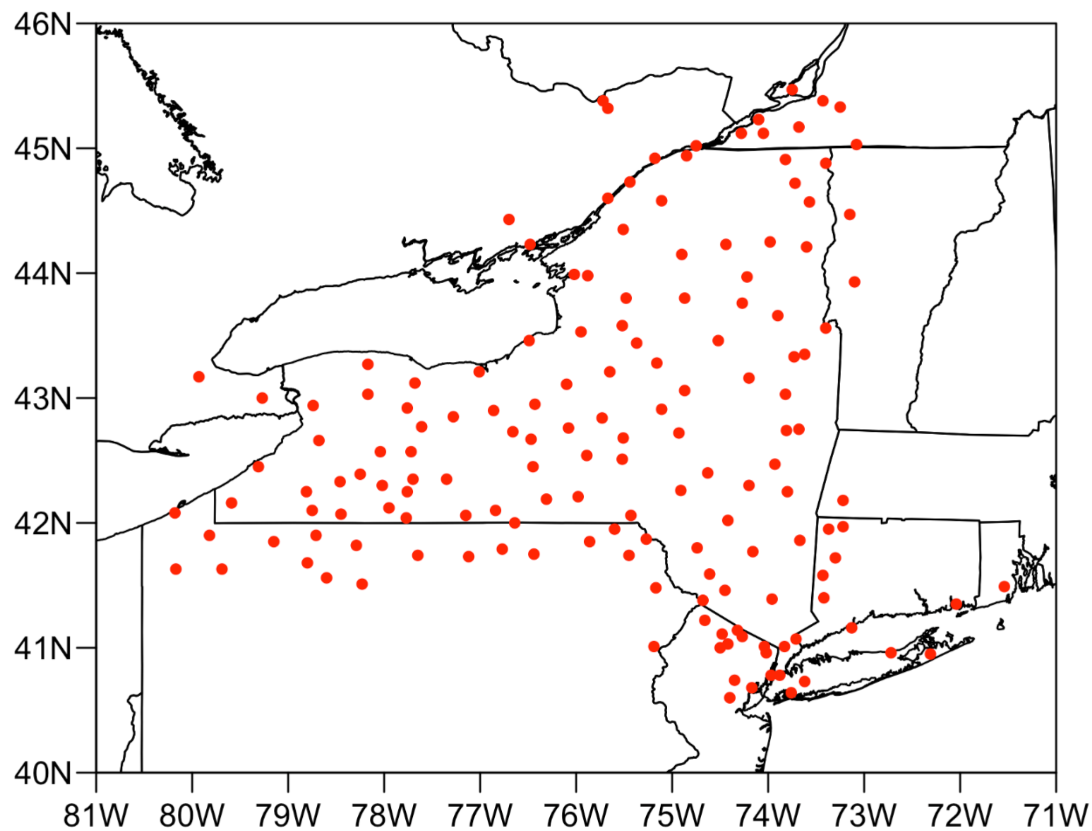

Figure 1: Map showing the locations of the 157 NWS COOP stations used in this study.

Model Data

Historical and future model output were obtained from two sources: 1) the Coordinated Regional Climate Downscaling Experiment (CORDEX; Jones et al. 2011), and 2) Phase 5 of the Coupled Model Intercomparison Project (CMIP5; Taylor et al. 2012). The CORDEX simulations consist of regional climate models (RCMs) run at approximately 50-km resolution and driven by atmosphere–ocean general circulation models (AOGCMs) from the CMIP5 project. Gridded daily precipitation estimates were extracted from four CORDEX model combinations and 25

CMIP5 models (Appendix B) for one historical climate scenario and two future climate scenarios (RCP4.5 and RCP8.5). The two future climate scenarios refer to different magnitudes ($W\ m^{-2}$) of net radiative forcing expected by 2100, relative to pre-industrial conditions. In addition to daily precipitation output, 6-hourly gridded atmospheric data were extracted from 20 CMIP5 models for comparison with the 6-hourly NCEP–NCAR reanalysis data.

Historical Precipitation Extremes

Partial Duration Series

In order to compute historical recurrence interval precipitation amounts, it was necessary to construct extreme precipitation distributions at each station. Following the method of Wilks and Cember (1993), partial duration series (PDS) of the *n* largest independent daily precipitation events were obtained for each station during the 1970–1999 period. Here, *n* is the largest integer not exceeding the number of days with valid precipitation observations divided by 365.25, and thus approximates the number of years of valid data at each station. To be considered independent, any two chronologically successive PDS events must be separated by at least seven calendar days. PDS were chosen to represent extreme precipitation events because they are commonly used to calculate recurrence interval precipitation amounts for engineering design purposes. While other studies have relied on annual maximum series (AMS) to calculate recurrence interval precipitation amounts, PDS are preferable because two or more of a station's largest daily precipitation events may occur during the same calendar year. By definition, AMS consist only of the single largest daily precipitation event from each year, and thus may exclude additional large precipitation events.

Extreme Value Fitting

After PDS were constructed for each station, precipitation amounts corresponding to 2-, 5-, 10-, 25-, 50-, and 100-year return periods were computed using two statistical fitting methods. The first method, hereafter referred to as the Beta-P method, employs the Levenberg-Marquardt method (Press et al. 1986) of maximum likelihood estimation to fit the Beta-P distribution (Mielke and Johnson 1974) to each station's PDS. Wilks (1993) examined several candidate probability distributions for estimating precipitation extremes and concluded that the Beta-P distribution best captured the extreme right tail of precipitation events in the northeastern U.S. The second method, hereafter referred to as the L-moments approach, first groups stations together based on similarities in their extreme precipitation distributions, and then applies L-moments regional frequency analysis (Hosking and Wallis 1997) to estimate precipitation extremes at individual stations in each group. Station groups were determined by performing a two-sample Kolmogorov–Smirnov (K–S) test on the PDS cumulative distribution functions (CDFs) at different pairs of stations (DeGaetano 1998). Finally, a generalized extreme value (GEV) distribution was fit to each station's PDS, with regionally averaged shape and scale parameters specified for all stations in a given group. The NWS is currently using L-moments regional frequency analysis to create a revised precipitation-frequency atlas (i.e., NOAA Atlas 14) for the entire United States (Perica et al. 2013). As Figure 2 illustrates, the Beta-P and L-moments approaches yield very similar values at shorter return periods. At longer return periods, the two fitting methods may yield large differences, with the Beta-P values often exceeding the L-moments values.

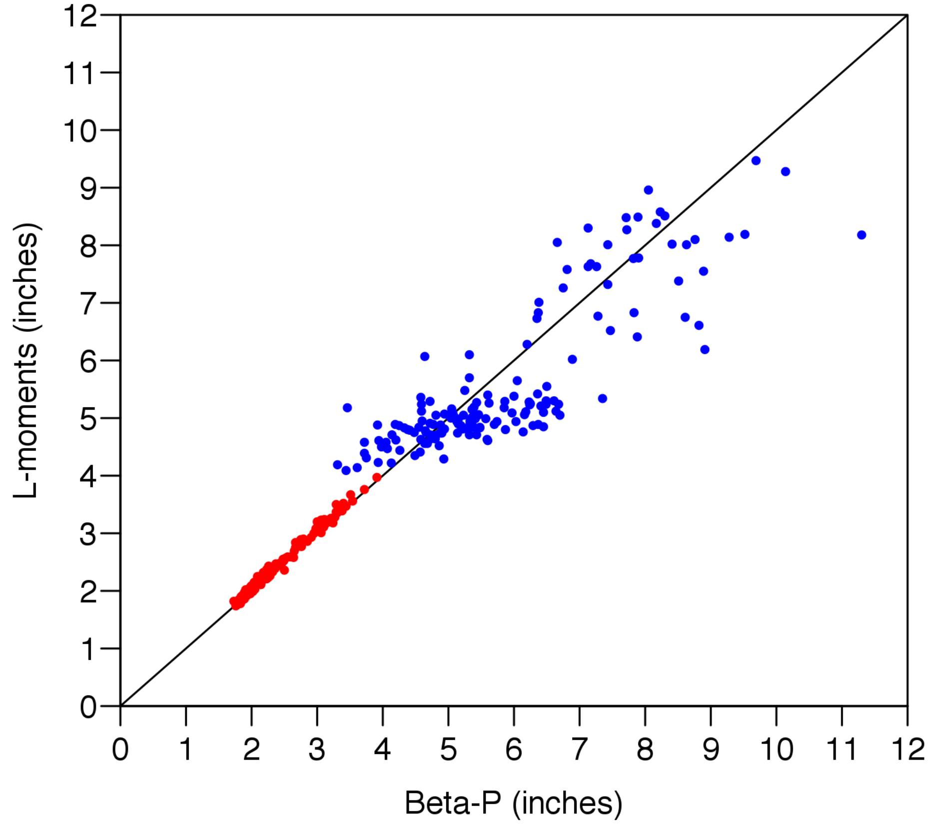

Figure 2: Daily 5-year (red) and 100-year (blue) recurrence interval precipitation amounts computed for the 1970–1999 period at all 157 COOP stations.

Confidence Intervals

One important caveat that must be considered when computing recurrence interval precipitation amounts is the discrepancy between the return period and the length of the data record. For example, this study estimates precipitation amounts corresponding to 100-year return periods, but uses data from significantly shorter 30-year periods. Therefore, computation of the 100-year recurrence interval precipitation amounts requires extrapolation beyond the length of the data record, and thus introduces a greater degree of uncertainty. One way to account for the uncertainty in recurrence interval precipitation amounts is to introduce confidence intervals, or bounds which represent the range of statistically likely values based on a given number of samples. For the purpose of this study, 90% confidence intervals for all recurrence interval precipitation amounts were estimated by randomly selecting (with replacement) *n* precipitation amounts from each station's PDS 1000 times. After computing the Beta-P and L-moments recurrence interval precipitation amounts for each of these 1000 trials, the 5th and 95th percentile values were chosen to represent to lower and upper confidence interval bounds, respectively. One noteworthy finding from the confidence interval calculations is that the confidence intervals for the Beta-P precipitation extremes are considerably larger than the confidence intervals for the

L-moments precipitation extremes at longer return periods. This finding suggests that the parameters of the Beta-P distribution are very sensitive to changes in the PDS sample.

Intensity Duration Frequency Curves

Once the daily recurrence interval precipitation amounts were obtained for each station, it was possible to develop intensity–duration–frequency (IDF) curves. By definition, an IDF curve conveys the relationship between precipitation intensity and duration for a specified return period. Water resources engineering heavily relies upon IDF curves to prevent or mitigate flooding associated with extreme precipitation. For the purpose of this study, 1-, 2-, 3-, 6-, 12-, 18, and 24-hour durations were used to construct IDF curves for 2-, 5-, 10-, 25-, 50-, and 100-year return periods. Sub-daily recurrence interval precipitation amounts were estimated by applying empirical adjustment factors to the daily recurrence interval precipitation amounts (McKay and Wilks 1995). After sub-daily recurrence interval precipitation amounts were calculated for each return period, a log-log regression was fit to the intensity–duration relationship in order to create smoothed IDF curves and interpolate recurrence interval precipitation amounts at intermediate durations. IDF curves were also generated for the lower and upper confidence interval bounds of each station's recurrence interval precipitation amounts. Figure 3 shows sample Beta-P and L-moments IDF curves corresponding to a 100-year return period at Albany, NY.

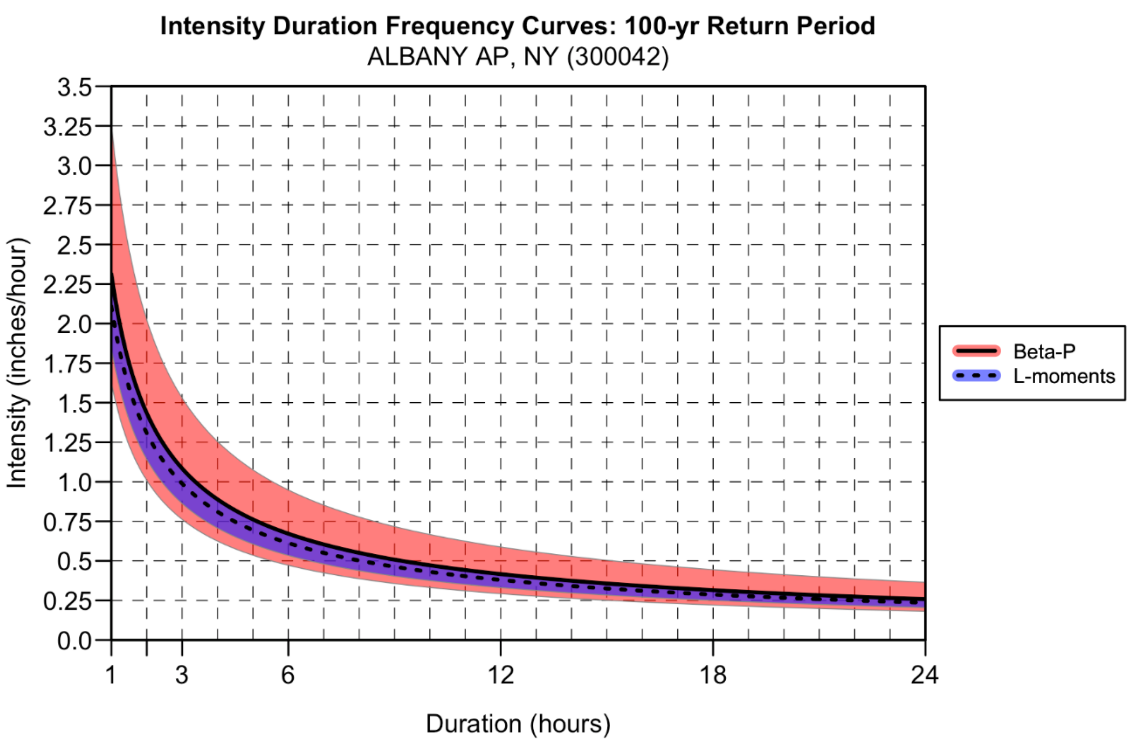

Figure 3: Historical IDF curves for the 100-year return period at Albany, NY. The solid (dashed) black line and red (blue) shaded region denote the Beta-P (L-moments) values and corresponding 90% confidence intervals.

Comparison with NOAA Atlas 14

Historical precipitation extremes estimated from the L-moments approach were compared to those given by NOAA Atlas 14 at the 98 New York stations. This supplemental analysis was motivated by the fact that many recent statewide and local impact studies have chosen to adopt the NOAA Atlas 14 precipitation thresholds as the standard historical reference values. Although NOAA Atlas 14 also employs L-moments regional frequency analysis to compute return period precipitation amounts, there are two key differences between NOAA Atlas 14 and the NRCC methodology. First, NOAA Atlas 14 uses the entire precipitation data record available at each station, whereas the NRCC approach specifies a 30-year historical period (1970–1999) for all stations. Second, NOAA Atlas 14 carries out the regionalization procedure on a station-by-station basis (i.e., the regions are defined with respect to each station), whereas the NRCC approach finds homogeneous regions and specifies regionally averaged shape and scale parameters for all stations in the same region. Thus, it was necessary to evaluate differences between the NRCC extreme precipitation estimates and the NOAA Atlas 14 extreme precipitation estimates. Figure 4 illustrates the bias (defined as the ratio between the NRCC and NOAA Atlas 14 values) in 2-, 5-, 10-, 25-, 50-, and 100-year return period precipitation amounts for a 24-hour event duration. In general, the differences between the NRCC values and the NOAA Atlas 14 values are quite small. The median station bias varies between 0.96 and 1.05, and the percent difference between NRCC and NOAA Atlas 14 values is consistently less than 10% for at least 50% of the 98 New York stations. Furthermore, all NRCC values fell within the confidence interval bounds of the NOAA Atlas 14 values.

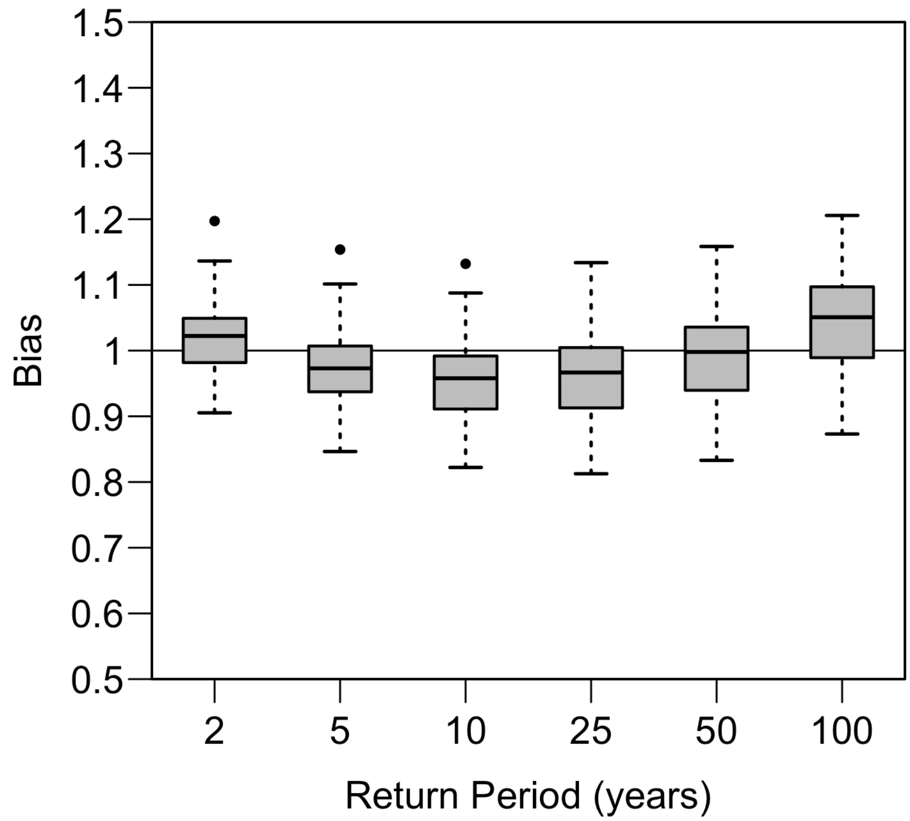

Figure 4: Boxplots showing bias in return period precipitation amounts estimated from the NRCC regionalized L-moments approach (with respect to the NOAA Atlas 14 values). Each boxplot consists of 98 unique station values.

Downscaling Procedures

Recent studies have used GCM projections to predict future changes in high-impact weather events such as extreme precipitation. While such impact studies are often conducted for point locations or fine-scale grids within a limited geographical domain, GCMs typically simulate atmospheric variables at horizontal resolutions of 100 km or greater (Wilby and Wigley 1997; Wilby et al. 2004). Unfortunately, these spatial resolutions are too coarse to adequately resolve certain orographic features and atmospheric processes that influence precipitation (Benestad 2010; Eden and Widmann 2014). The discrepancy in spatial scales between climate model resolution and impact area is addressed through the process of downscaling. In climate science, downscaling refers to any technique by which local-scale climate information is derived from coarse-scale model output or reanalysis data. Downscaling methods are generally grouped into two broad categories: statistical and dynamical. Statistical downscaling utilizes empirical relationships between large-scale atmospheric variables (predictors) and local surface variables (predictands) to predict local weather conditions or events. Dynamical downscaling involves running a nested high-resolution model (usually an RCM) with boundary conditions specified by a coarse-scale AOGCM. For the purpose of this study, three different downscaling methods were used to estimate future daily precipitation extremes at each station. A detailed methodology for each downscaling method is explained below.

Dynamical Downscaling

The first method employs quantile–quantile mapping (Panofsky and Brier 1968) to bias correct areally adjusted daily precipitation extremes from the dynamically downscaled CORDEX simulations. Daily precipitation estimates at each station were obtained by calculating the distance-weighted averages of simulated daily precipitation totals over the nearest four grid cells. Next, PDS of the largest daily precipitation estimates at each station were constructed for one historical period (1970–1999) and three future periods (2010–2039, 2040–2069, and 2070–2099), and the Beta-P and L-moments approaches were used to compute the corresponding recurrence interval precipitation amounts. Because the simulated recurrence interval precipitation amounts were derived from daily precipitation totals averaged over 50-km grid cells, areal reduction factors (ARFs) were necessary to convert gridded precipitation to point values of precipitation. ARFs for all return periods were estimated according to Equation (1), where t is the precipitation duration (h), A is the grid area (units of 1000 km^2), and a, b, and c are empirically derived coefficients based on 24-hour precipitation durations (Allen and DeGaetano 2005). Model biases were determined by computing the ratios between the ARF-adjusted recurrence interval precipitation amounts and the observed recurrence interval precipitation amounts during the historical period. Assuming that model biases would remain constant with time, the inverses of the individual bias values were taken as factors needed to bias correct the projected future recurrence interval precipitation amounts. Final future downscaled precipitation extremes were estimated by applying these bias correction factors to the ARF-adjusted future recurrence interval precipitation amounts.

$$\mathrm{ARF} = 1 - \exp\left(at^b\right) + \exp\left(at^b - cA\right) \tag{1}$$

Delta Method

The second method, a variation of the delta method, computes differences in simulated precipitation extremes between AOGCM future and historical periods, and simply applies these differences toward observed precipitation extremes. As in the previous method, daily precipitation estimates at each station were obtained by calculating the distance-weighted averages of simulated daily precipitation totals over the nearest four grid cells. Next, PDS of the largest daily precipitation estimates at each station were constructed for the historical and future periods, and the Beta-P and L-moments approaches were used to compute the corresponding recurrence interval precipitation amounts. Unlike the previous method, ARFs were not used to convert areally averaged precipitation to point values of precipitation due to the coarse resolution of the AOGCM output. Instead, future downscaled recurrence interval precipitation amounts were estimated by calculating the percent changes in simulated precipitation extremes between the historical and future periods, and applying these percent change factors to observed recurrence interval precipitation amounts. In order to test the sensitivity of percent change factors to model resolution, an "upscaling" experiment was conducted using output from the CORDEX simulations. The original horizontal resolution of the CORDEX output was reduced from 50 km to 100 km, 150 km, and 200 km by taking the combined mean of simulated daily precipitation totals from neighboring grid cells. In essence, daily precipitation estimates for each 100-km, 150-km, and 200-km grid cell represented a combination of a 2 × 2, 3 × 3, or 4 × 4 set of 50-km grid cell values, respectively. This upscaling experiment revealed no discernable relationship between the magnitude of percent change and grid cell resolution.

Analog Method

The third method combines quantile–quantile mapping with a unique approach for downscaling daily precipitation extremes from historical analogs. Generally speaking, analog methods identify historical large-scale weather patterns similar to the large-scale weather pattern on a given target day, and then use local weather conditions observed on the historical analog day(s) to predict local weather conditions on the target day. The particular analog approach employed in this study involves a multi-step procedure in which the occurrence of extreme precipitation on a given model day is first predicted based on the observed probability of extreme precipitation on that day's 30 closest historical analog days. Then, if extreme precipitation occurred on a randomly selected analog day from this 30-day subset, precipitation observations associated with the selected analog day were used to ascribe precipitation amounts to individual stations on the corresponding model day.

Model days and candidate analog days were compared to one another by calculating standardized root mean squared error (RMSE) values for three predictor variables over the 20°N, 105°W – 55°N, 50°W bounding box. The three predictor variables – 850-hPa relative vorticity, total precipitable water (TPW), and vertically integrated water vapor transport (IVT) – were chosen to represent synoptic-dynamic processes and thermodynamic environments commonly associated with heavy precipitation and flash flooding in the United States (Maddox et al. 1979; Heideman and Fritsch 1988; Winkler 1988; Konrad 1997; Kunkel et al. 2012; Gao et al. 2014). Predictor fields on the candidate analog days were derived from 6-hourly NCEP–NCAR reanalysis, whereas predictor fields on the model days were derived from 6-hourly CMIP5 model output. Before computing the predictor variables, the raw CMIP5 data were horizontally re-gridded and vertically interpolated to match the horizontal and vertical resolution of NCEP–NCAR reanalysis. The RMSE calculation for a model day–candidate analog day pair is given by Equation (2), where P_{ik} (P_{jk}) represents the value of predictor "P" on model day x_i (analog day x_j), at grid point "k", and N is the total number of grid points. Squared error values at a given grid point "k" were adjusted by a weighting factor (W_k) dependent on that grid point's proximity to the study domain (Figure 5). Standardization of RMSE values was achieved by comparing the actual RMSE values with reference populations of RMSE from 1,000,000 randomly sampled pairs of days, and locating the centiles of the reference RMSE populations nearest the actual RMSE values. For a given model day, the 30 closest historical analogs thus represent the candidate analog days with the 30 smallest standardized RMSE averaged across all three predictor variables.

$$\mathrm{RMSE_P}(x_i,x_j) = \sqrt{\frac{\sum_{k=1}^{N}\left(P_{ik}-P_{jk}\right)^2 \cdot W_k}{\sum_{k=1}^{N} W_k}} \tag{2}$$

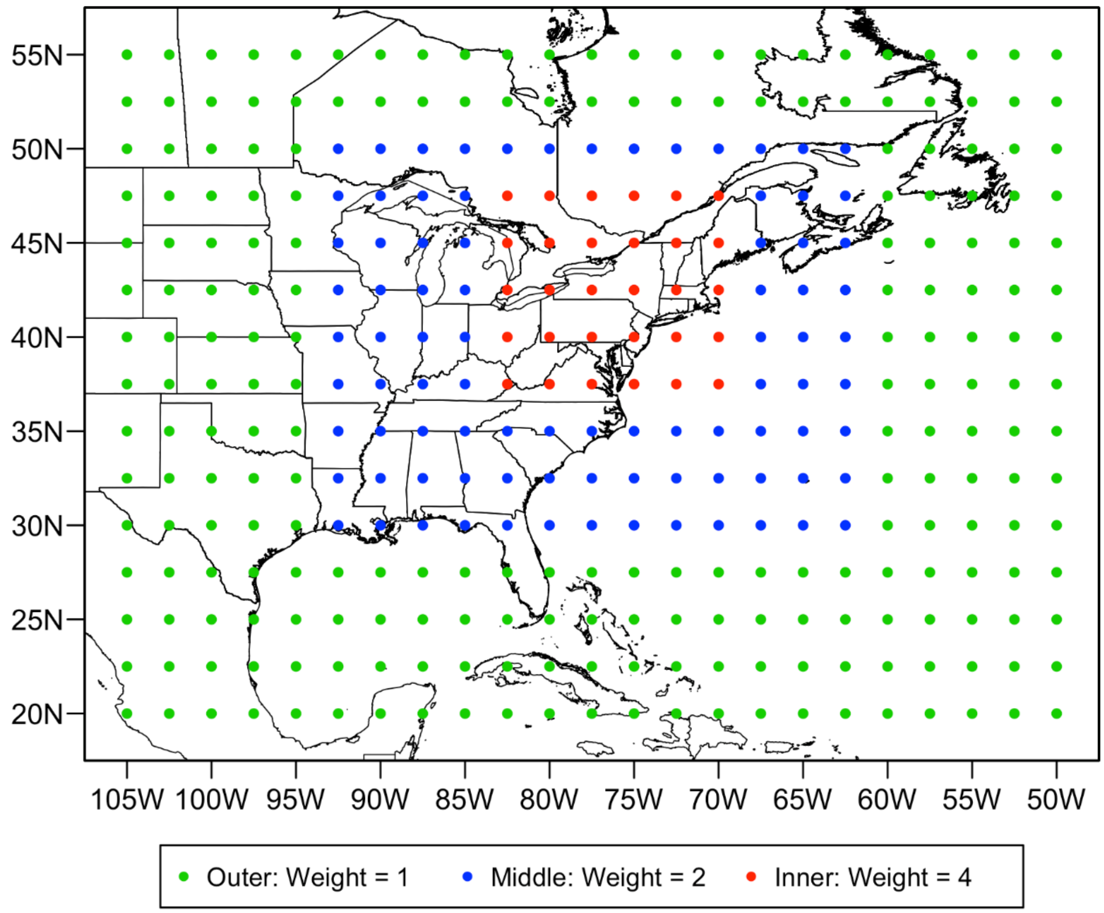

Figure 5: Map illustrating the weighting factors for each reanalysis grid point.

After finding a given model day's 30 closest historical analogs, one of these analog days was randomly selected based on each analog day's relative degree of similarity to the model day. In order to translate the analog pattern to station precipitation, the 157 COOP stations were partitioned into distinct clusters based on how regularly different pairs of stations received extreme precipitation from the same meteorological event during the 1961–2010 period. For each unique pair of stations, the fraction of non-concurrent PDS events [i.e., the fraction of PDS events at Station A that did not occur on the same day, the previous day, or the next day at Station B (and vice versa)] during the 1961–2010 period was obtained as a measure of dissimilarity between the two stations. These dissimilarity measures were used to construct a 157 × 157 distance matrix, and Ward's method of hierarchical clustering (Ward 1963) was applied to this distance matrix to identify distinct station groups. The resulting station clusters (Figure 6) thus represent the spatiotemporal variability in extreme precipitation across the study domain.

Next, it was determined whether or not extreme precipitation occurred at any stations in each cluster on the selected analog day. If only one station recorded a PDS event on the selected analog day, the previous day, or the next day, the corresponding daily precipitation amount was randomly assigned to one station in the cluster. The probability of assigning this precipitation amount to a particular station was quantified as the percentage of cluster-specific single-station events occurring at that station during the 1961–2010 period. If multiple stations recorded a PDS event on the selected analog day, the previous day, or the next day, each station's maximum daily precipitation observation over the 3-day period was extracted, and these maximum daily precipitation observations were ascribed to all stations in the cluster. The largest daily precipitation amount was always assigned separately based the climatological probability that each station received the largest daily precipitation amount during a multi-station event. All remaining maximum daily precipitation amounts were purely randomly assigned to the remaining stations in that cluster. If no stations in the cluster experienced a PDS event on the selected analog day, no precipitation amounts were assigned.

After running through all model days in each 30-year period, new PDS were constructed from the precipitation amounts assigned to each station, and the Beta-P and L-moments approaches were used to compute the corresponding recurrence interval precipitation amounts. In order to minimize the effect of selecting one historical analog for each model day, the process of randomly selecting historical analogs, ascribing precipitation amounts, and computing recurrence interval precipitation amounts was repeated 1000 times. The median values of the 1000 Beta-P and L-moments precipitation threshold populations were chosen to represent the final downscaled precipitation threshold estimates. Similar to the dynamically downscaled projections, the future downscaled precipitation extremes were adjusted by bias correction factors calculated from a comparison of the historical downscaled recurrence interval precipitation amounts and the observed recurrence interval precipitation amounts.

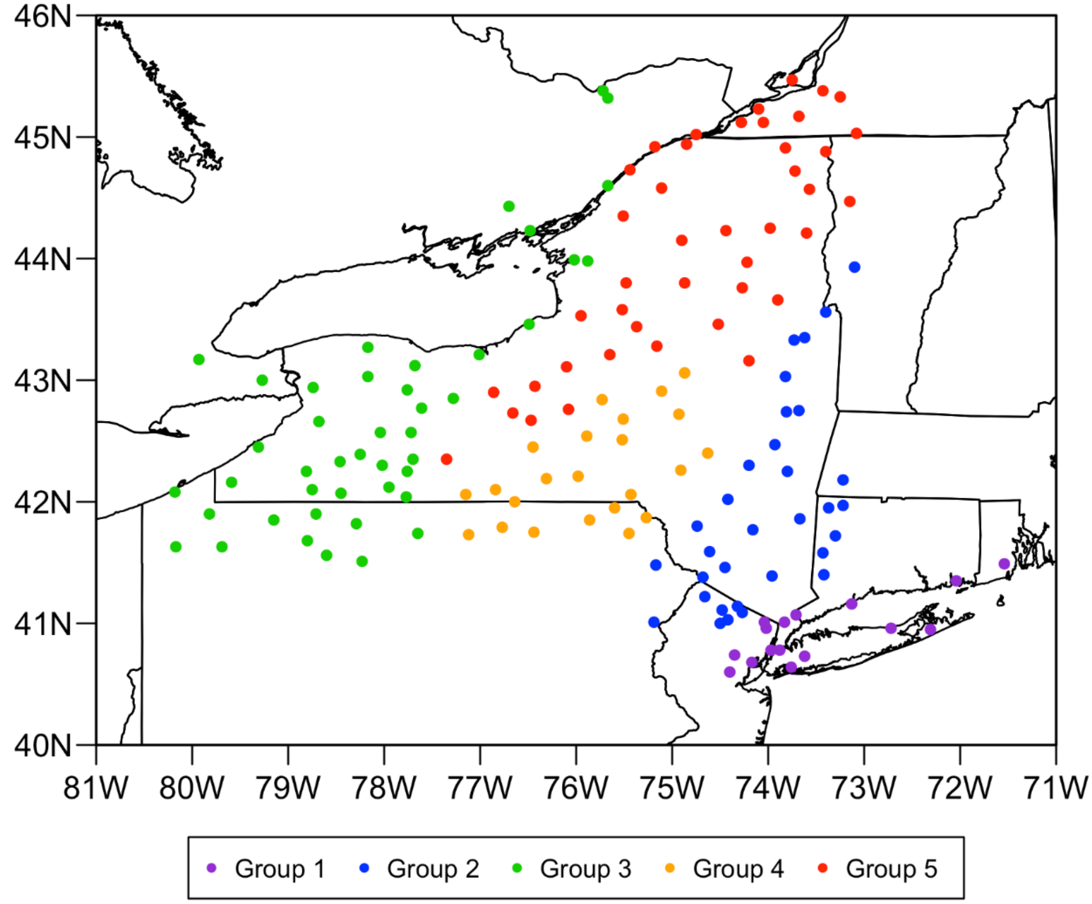

Figure 6: Map illustrating the five spatiotemporal clusters used to translate the analog pattern to station-based precipitation.

Uncertainty Analysis

After obtaining final extreme precipitation projections from each downscaling procedure, it was possible to evaluate the variability in future projections amongst the different downscaling method–climate model combinations. In total, 49 unique sets of extreme precipitation projections were generated for each climate scenario–time period combination at each station. The 49 individual projections thus form a 49-member ensemble of future recurrence interval precipitation amounts for a specified station, climate scenario, and time period. A statistical summary of future projections was completed by calculating the ensemble mean recurrence interval precipitation amounts, as well as the precipitation threshold values corresponding to the 10^{th}, 25^{th}, 50^{th}, 75^{th}, and 90^{th} percentiles of the 49 projections. These percentile values may alternately be expressed in terms of exceedance/non-exceedance probability. For instance, if the 10^{th} percentile value of the 100-year storm is 4.00 in, there is a 90% (10%) probability that the future magnitude of the 100-year storm will be greater than (less than) 4.00 in.

Results

Historical Bias

Before creating downscaled extreme precipitation projections for the future climate scenarios, it was necessary to examine the ability of the various downscaling method–climate model combinations to generate realistic estimates of historical precipitation extremes. More specifically, model biases were evaluated by comparing the downscaled historical recurrence interval precipitation amounts with the observed recurrence interval precipitation amounts during the 1970–1999 period. Here, bias is defined as the ratio between the downscaled and observed recurrence interval precipitation amounts for a specified return period. Since the delta method uses raw CMIP5 daily precipitation output, historical biases were computed for the dynamical downscaling and analog downscaling methods only.

Figures 7–10 show boxplots of ensemble mean and individual model biases in 5-year and 100-year recurrence interval precipitation amounts estimated from the dynamical downscaling and analog downscaling methods. Overall, both methods yield realistic estimates of 5-year and 100-year recurrence interval precipitation amounts at most stations. One key difference between the two downscaling methods is that, on average, the dynamical downscaling method slightly overestimates the 5-year and 100-year recurrence interval precipitation amounts (Figures 7 and 8), whereas the analog downscaling method slightly underestimates the 5-year and 100-year recurrence interval precipitation amounts (Figures 9 and 10). The tendency of the analog downscaling method to underestimate precipitation extremes is most pronounced for 100-year recurrence interval precipitation amounts computed from the L-moments approach. In both downscaling methods, the range of model biases computed from the Beta-P approach increases with return period, suggesting that the Beta-P approach is quite sensitive to return period length. In other words, small differences in the PDS distribution may yield comparatively large differences in recurrence interval precipitation amounts computed from the Beta-P approach at longer return periods. Due to concerns over the Beta-P method's sensitivity to return period length, the decision was made to exclude any future extreme precipitation projections computed using the Beta-P approach.

Figure 11 illustrates the spatial variability of ensemble mean bias in 5-year and 100-year recurrence interval precipitation amounts estimated from the two downscaling methods using the L-moments approach. The dynamical downscaling method overestimates 5-year and 100-year recurrence interval precipitation amounts throughout much of New York State, with the largest wet biases concentrated over the western Finger Lakes and the Adirondacks. Notable exceptions include the lower and middle Hudson Valley, as well as Long Island and New York City, where the dynamical downscaling method consistently underestimates the 5-year and 100-year recurrence interval precipitation amounts. By comparison, the analog downscaling method underestimates 5-year recurrence interval precipitation amounts throughout much of New York State, with exceptions in parts of northeastern New York, western New York, and the St. Lawrence Valley. This dry bias is larger and more widespread for the 100-year recurrence interval precipitation amounts.

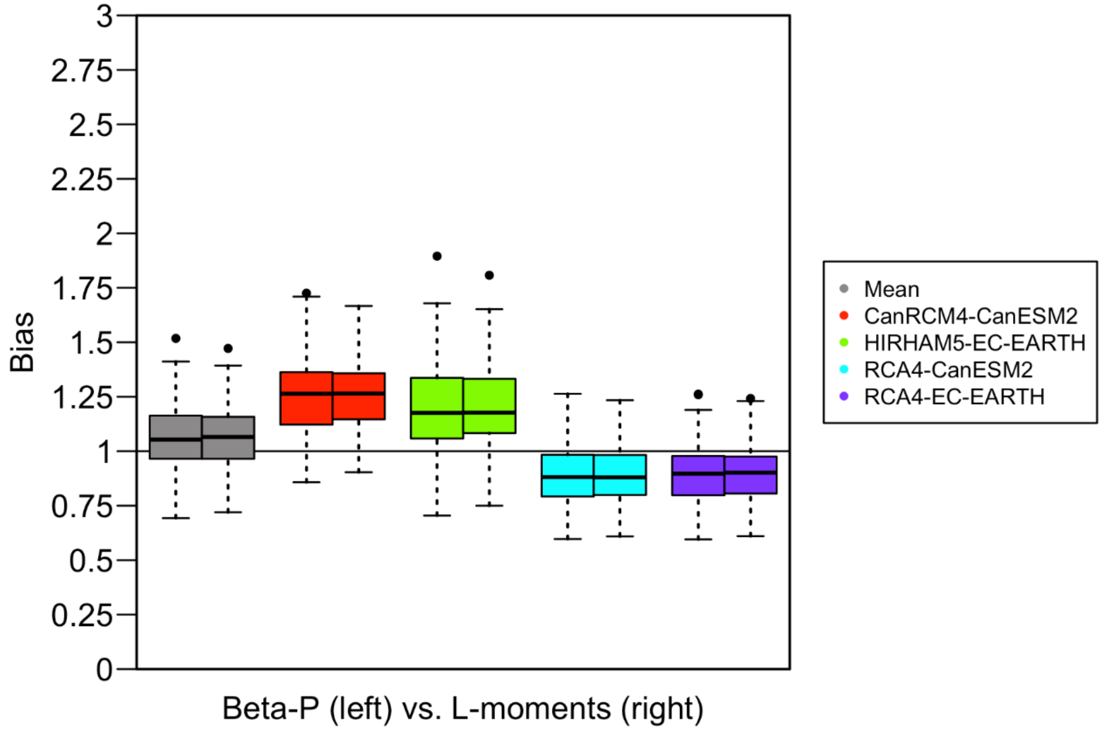

Figure 7: Boxplots showing bias in 5-year return period precipitation amounts estimated from the dynamical downscaling method. Each boxplot consists of 157 unique station values.

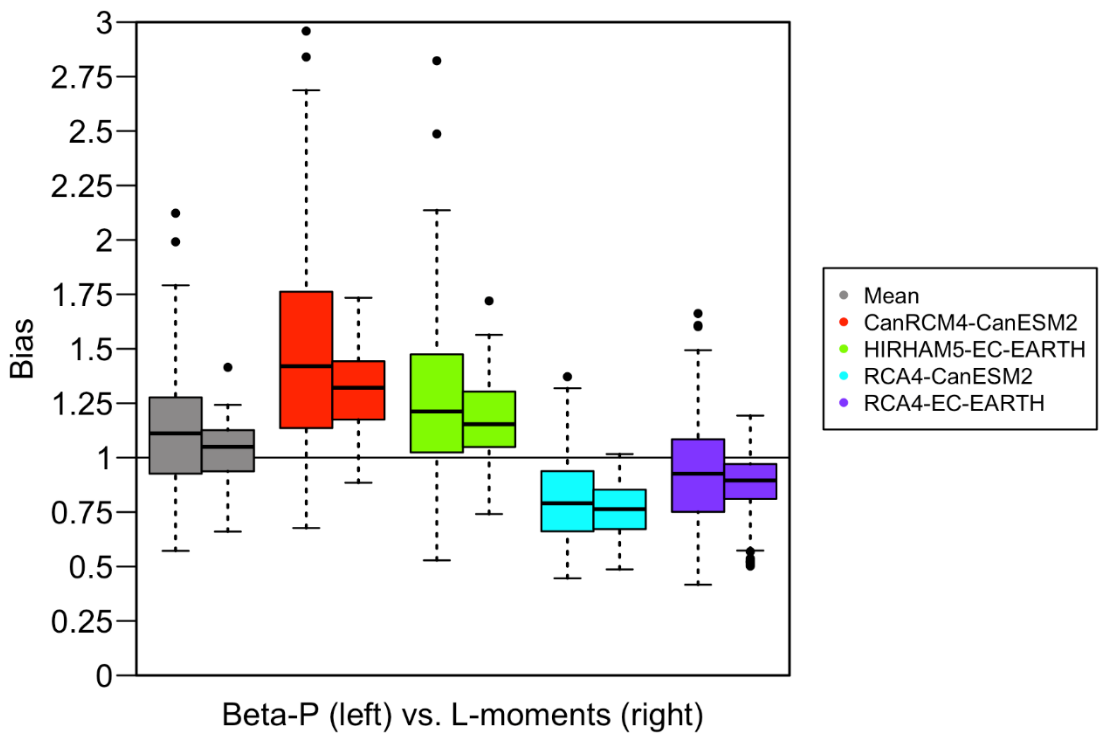

Figure 8: As in Figure 7, except for the 100-year return period.

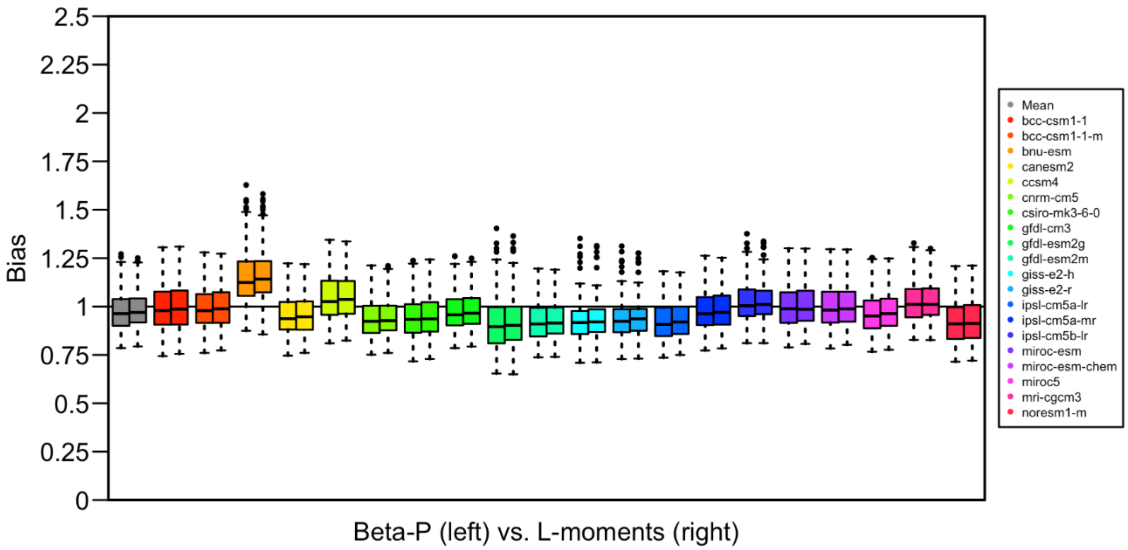

Figure 9: Boxplots showing bias in 5-year return period precipitation amounts estimated from the analog downscaling method. Each boxplot consists of 157 unique station values.

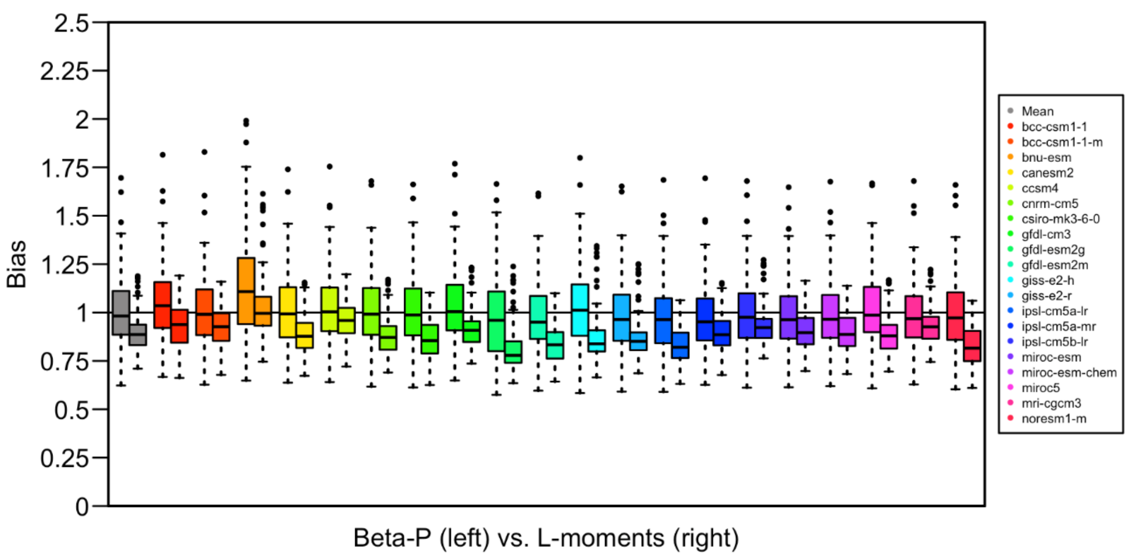

Figure 10: As in Figure 9, except for the 100-year return period.

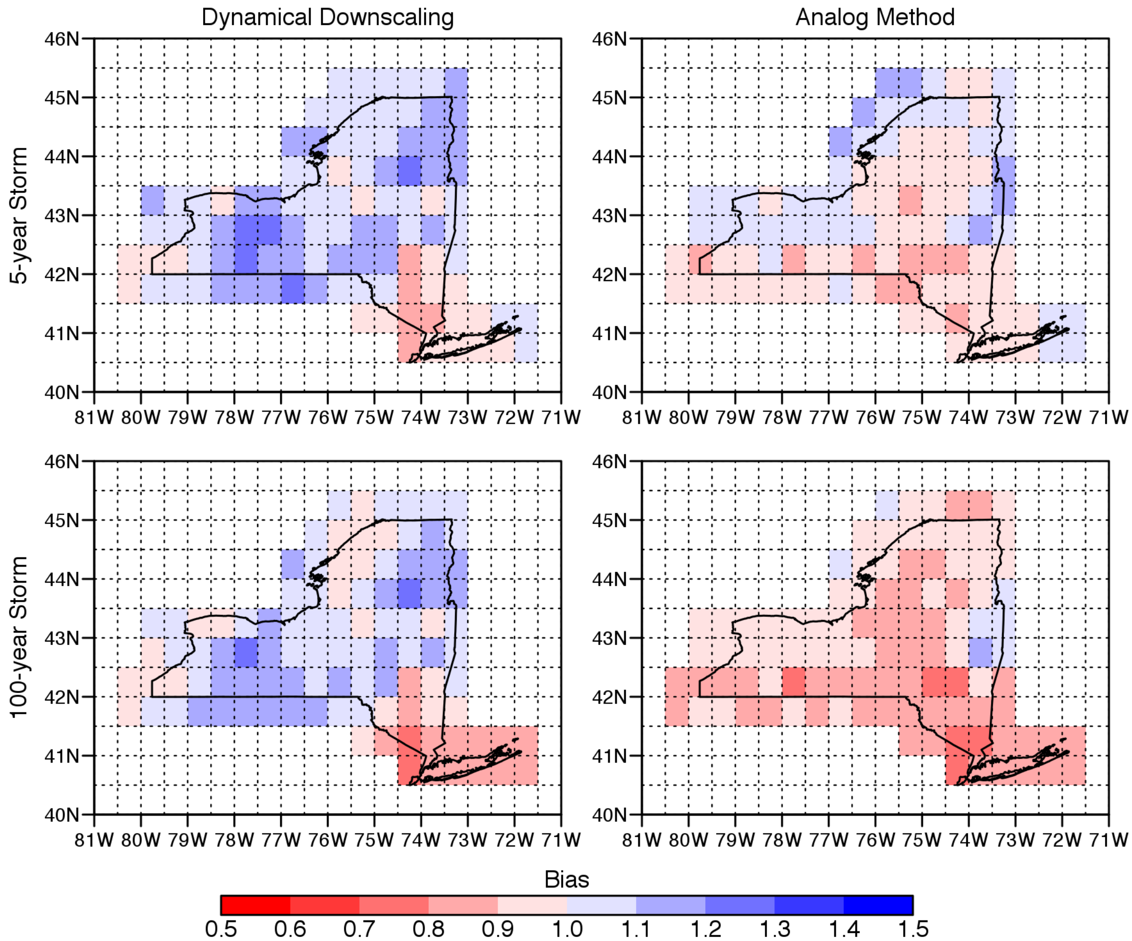

Figure 11: Gridded maps showing the mean bias in 5-year (top) and 100-year (bottom) return period precipitation amounts obtained from the dynamical downscaling method (left) and the analog method (right) for the 1970–1999 period. Grid cell values were estimated by interpolating the 157 station values to 0.5 × 0.5 grid cells.

Future Projections

Figure 12 shows boxplots of ensemble mean projected changes in 5-year and 100-year return period precipitation amounts for the three downscaling methods. In general, the three downscaling approaches yield similar results during the early 21st century, with median projected increases of 5–10 % across all 157 stations. As time progresses, the magnitude of the projected changes in 5-year and 100-year return period precipitation amounts increases, particularly during the late 21st century under the RCP8.5 scenario. Moreover, the differences between the three downscaling methods become progressively larger. By the late 21st century, the dynamical downscaling method consistently yields the greatest increases in return period precipitation amounts, whereas the analog method generally yields the smallest increases. These differences are especially pronounced under the RCP8.5 scenario, with the analog method (dynamical downscaling method) indicating a 10–15% (25–35%) increase in the magnitude of the 100-year storm. Lastly, the length of the boxplots suggests that the variability in projected changes among the 157 stations is substantially larger for the dynamical downscaling method than for the other two downscaling methods.

Gridded maps illustrating the spatial differences in ensemble mean projected changes in the 100-year return storm between the three downscaling methods are shown in Figure 13. By the late 21st century, all three downscaling methods yield statewide increases in the intensity of the 100-year storm. The magnitude of projected changes varies by downscaling method, climate forcing scenario, and location. Consistent with Figure 11, these maps indicate that the dynamical downscaling method (analog method) predicts the largest (smallest) increases in the intensity of the 100-year storm, and the projected changes are consistently larger under the RCP8.5 scenario than the RCP4.5 scenario. In terms of spatial variability, the delta method (analog method) predicts the largest (smallest) changes over southeastern New York and the smallest (largest) changes across sections of northern, western, and central New York. The spatial pattern of changes predicted by the dynamical downscaling method is less consistent and exhibits much greater spatial variability. While this result is likely an artifact of the very limited number of CORDEX simulations available, the higher resolution of the CORDEX simulations may also be partly responsible for the relatively large station-to-station variability.

Figure 14 illustrates the downscaling method–climate model uncertainty in projected changes in the 100-year storm. Here, the 10th (90th) percentile refers to the 10th (90th) percentile of the 49 unique downscaling method–climate model combinations. As Figure 13 suggests, the range of projected changes by the late 21st century is quite large. For instance, under the RCP4.5 scenario, the 10th (90th) percentile change in the 100-year storm ranges from -10% to +5% (+20% to 40%) statewide. Under the RCP8.5 scenario, the 10th (90th) percentile change in the 100-year storm ranges from -5% to +10% (+35% to +55%). By comparison, the mean projected changes in the 100-year storm under the RCP4.5 and RCP8.5 scenarios are on the order of +10–15% and +15–25%, respectively. Given the high degree of uncertainty in projected changes, it may be prudent to use a certain percentile value to assess flood vulnerability and risk of hydrologic failure rather than simply rely on the ensemble mean.

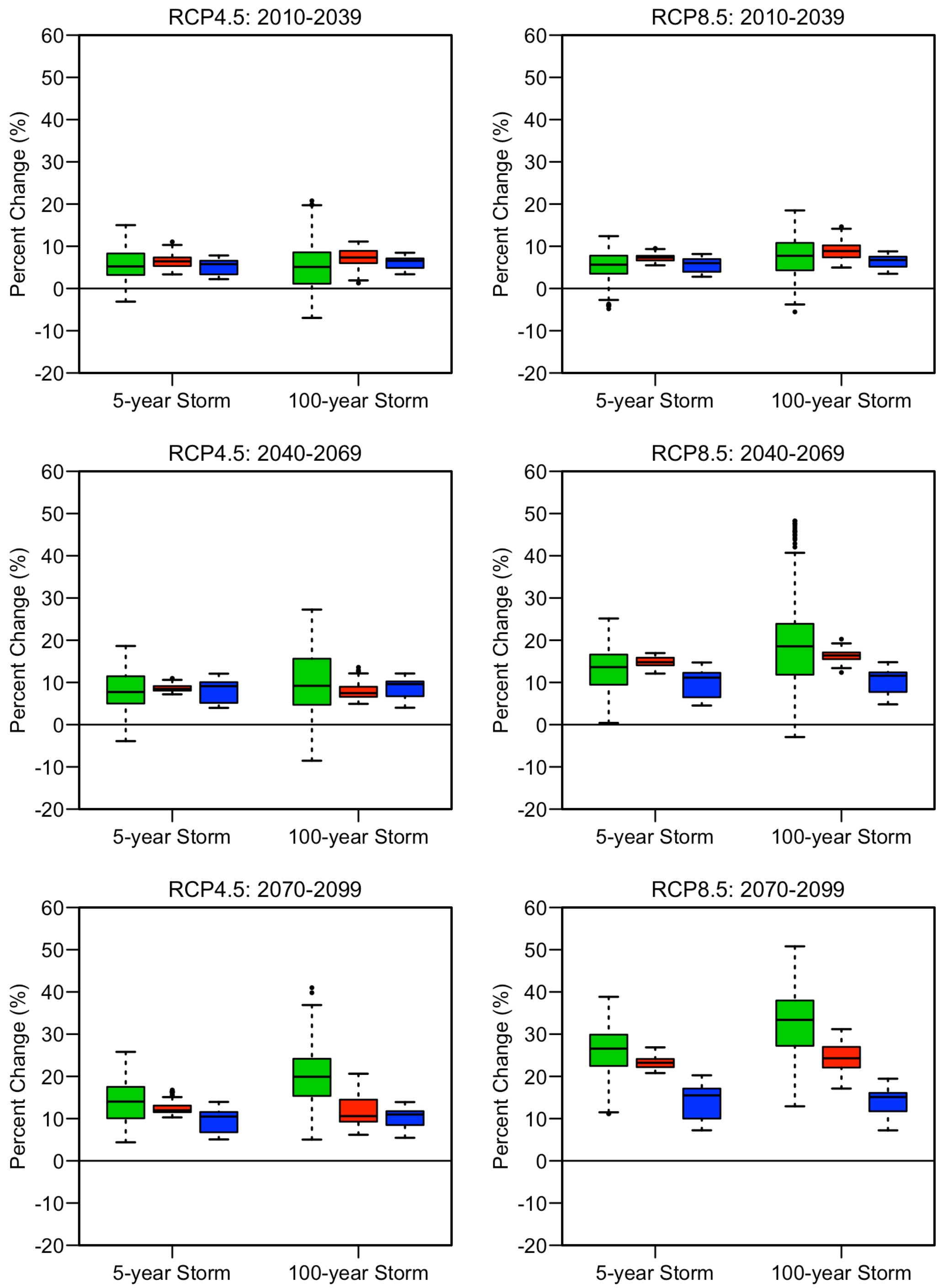

Figure 12: Boxplots illustrating mean percent changes in 5-year and 100-year return period precipitation amounts obtained from the dynamical downscaling method (green), the delta method (red), and the analog method (blue). Each boxplot consists of 157 unique station values.

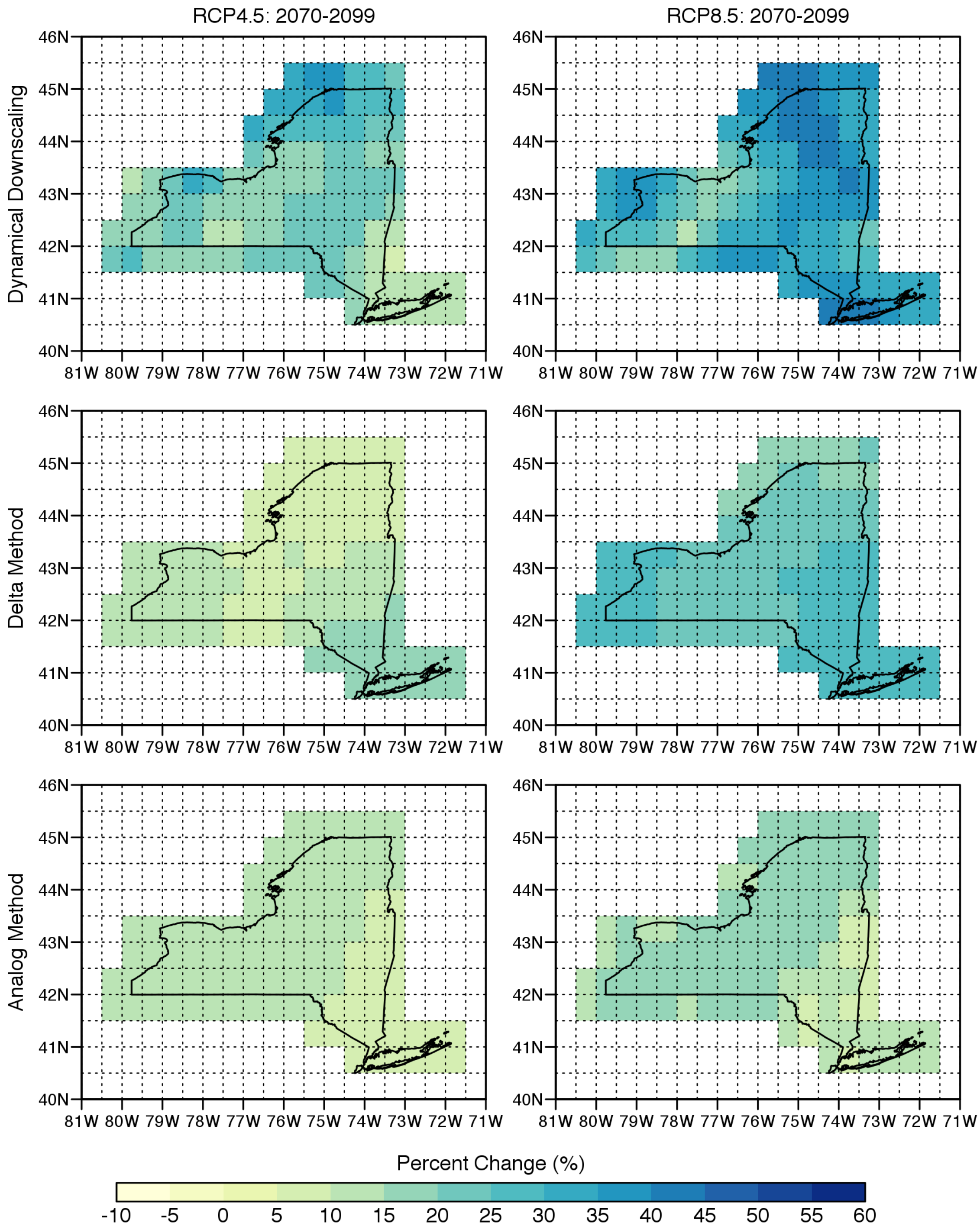

Figure 13: Gridded maps showing the mean percent change in 100-year return period precipitation amounts between the 1970–1999 period and the 2070–2099 period for the three downscaling methods and two RCP scenarios. Grid cell values were estimated by interpolating the 157 station values to 0.5 × 0.5 grid cells.

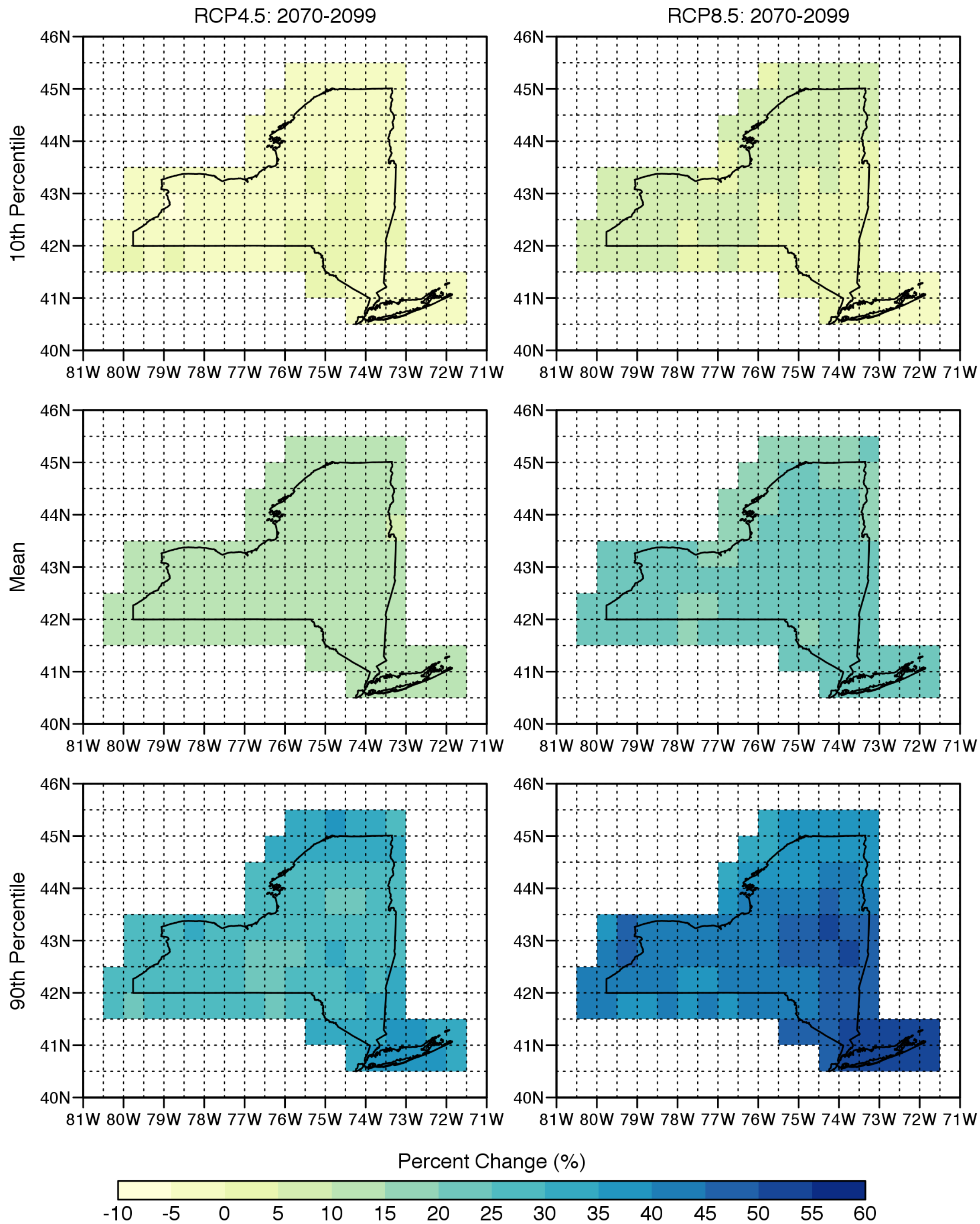

Figure 14: Gridded maps showing the 10th percentile, mean, and 90th percentile percent change in 100-year return period precipitation amounts between the 1970–1999 period and the 2070–2099 period for the two RCP scenarios (across all downscaling method–model combinations). Grid cell values were estimated by interpolating the 157 station values to 0.5 × 0.5 grid cells.

Website Products

Station-Specific IDF Curves

The first website product is an interactive tool that allows users to compare observed and projected IDF curves at a single station. Users must select a station and specify the return period (2, 5, 10, 25, 50, or 100 years), emissions scenario (RCP4.5 or RCP8.5), and future time period (2010–2039, 2040–2069, or 2070–2099). Additionally, users have the option of substituting the NRCC historical IDF curve with an IDF curve derived from the NOAA Atlas 14 precipitation estimates. The solid (dashed) black line denotes the future (historical) IDF curve. The red shaded region represents the range between the 10^{th} and 90^{th} percentile values of the future downscaled precipitation extremes. The blue shaded region represents the 90% confidence interval of the observed precipitation extremes. As noted above, the smoothed IDF curves were obtained by fitting a log-log regression to the intensity-duration relationship at major intervals of 1, 2, 3, 6, 12, 18, and 24 hours. The IDF viewer contains a scroll tool that allows users to navigate the IDF curves and provides estimated precipitation intensities at 6-minute intervals. A supplementary table shows the smoothed intensity values corresponding to 1-, 2-, 3-, 6-, 12-, 18-, and 24-hour durations. A sample screenshot of this product is shown in Figure 15.

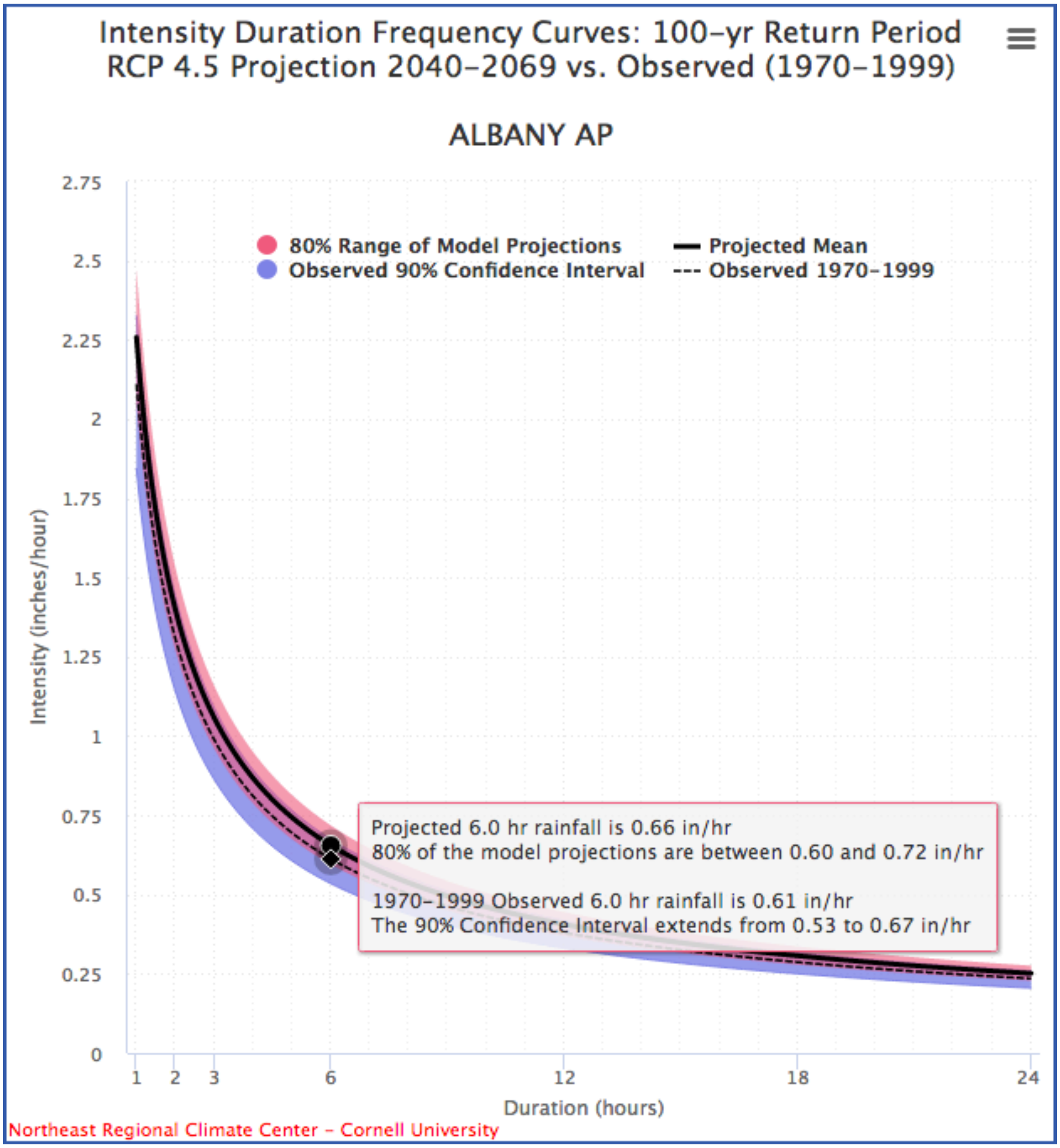

Figure 15: Smoothed IDF curves corresponding to the 100-year return period at Albany, NY. The solid (dashed) line denotes the historical (future) IDF curve. The blue shaded region represents the 90% confidence interval of the historical intensity-duration relationship. The red shaded region represents the range between the 10th and 90th percentiles of the future downscaled intensity-duration relationship.

Statewide Maps of Projected Changes

The second website product is a tool that generates statewide maps of projected changes in extreme precipitation. These maps are created by interpolating the 157 COOP station values to 0.5° × 0.5° grid cell values. Users must select the return period, emissions scenario, future time period, and ensemble member (10th percentile, mean, or 90th percentile). Additionally, users must specify the type of gridded map to be produced. The first map type shows the projected percent change in return period precipitation amounts between the historical period and the specified future period. The second map type shows the projected future recurrence interval of the precipitation threshold corresponding to the specified historical return period. For instance, if one selects a return period of 100 years, an output value of 50 suggests that the historical 100-year storm is expected to occur on average once every 50 years in the future. In other words, the annual exceedance probability of the historical 100-year storm increases from (0.01 to 0.02). Future recurrence intervals were estimated by computing the annual exceedance probabilities of the future 2-, 5-, 10-, 25-, 50-, and 100-year precipitation intensities from the historical L-moments distribution parameters [Equation (3)]. Next, these probabilities were converted to expected recurrence intervals [Equation (4)], and a log-log regression was fit between the expected recurrence intervals and the 2-, 5-, 10-, 25-, 50-, and 100-year reference return periods. The resulting slope and regression parameters were subsequently used to predict the future recurrence interval of the historical n-year storm [Equation (5)]. Regression parameters were calculated at each station for all six combinations of emissions scenario and future time period.

$$P_{HIST} = 1 - \exp\left[-\left(1 - \zeta \frac{x/i - \mu}{\sigma}\right)^{1/\zeta}\right] \tag{3}$$

$$R_{HIST} = 1/P_{HIST} \tag{4}$$

$$R_{FUT} = \exp[\beta \log(R_{HIST}) + \alpha] \tag{5}$$

In Equation (3), x is the future precipitation threshold (converted to a daily value), i is the index flood factor, ζ is the shape parameter, μ is the location parameter, and σ is the scale parameter. In Equation (5), β is the slope of the log-log regression, and α is the y-intercept of the log-log regression.

30-year Exceedance Probabilities

The last website product is a tool that estimates the historical and future probability of exceedance for a given precipitation intensity during a 30-year time period. Users must select a station and specify the event duration and total precipitation amount. Unlike annual exceedance probability, this value represents the probability that a precipitation event of a specified magnitude and duration is exceeded at least once during the entire period. Such information helps engineers, urban planners, ecologists, and emergency mangers better understand flood vulnerability and assess the risk of hydrologic failure. The probability of exceedance is given by:

$$P_e = 1 - \left[1 - \left(\frac{1}{T}\right)\right]^n \tag{6}$$

where T is the recurrence interval and n is the number of years in the period of interest. For historical exceedance probabilities, the recurrence interval was computed from Equations (3) and (4). For future exceedance probabilities, the recurrence interval was computed from Equations (3)–(5). The term in brackets denotes the annual non-exceedance probability, or the probability that a precipitation amount with recurrence interval T is not exceeded in a given year. Exceedance probabilities were also estimated for the historical 90% confidence interval bounds, as well as the 10th and 90th percentiles of the future downscaled projections. A sample screenshot of this product is shown in Figure 16.

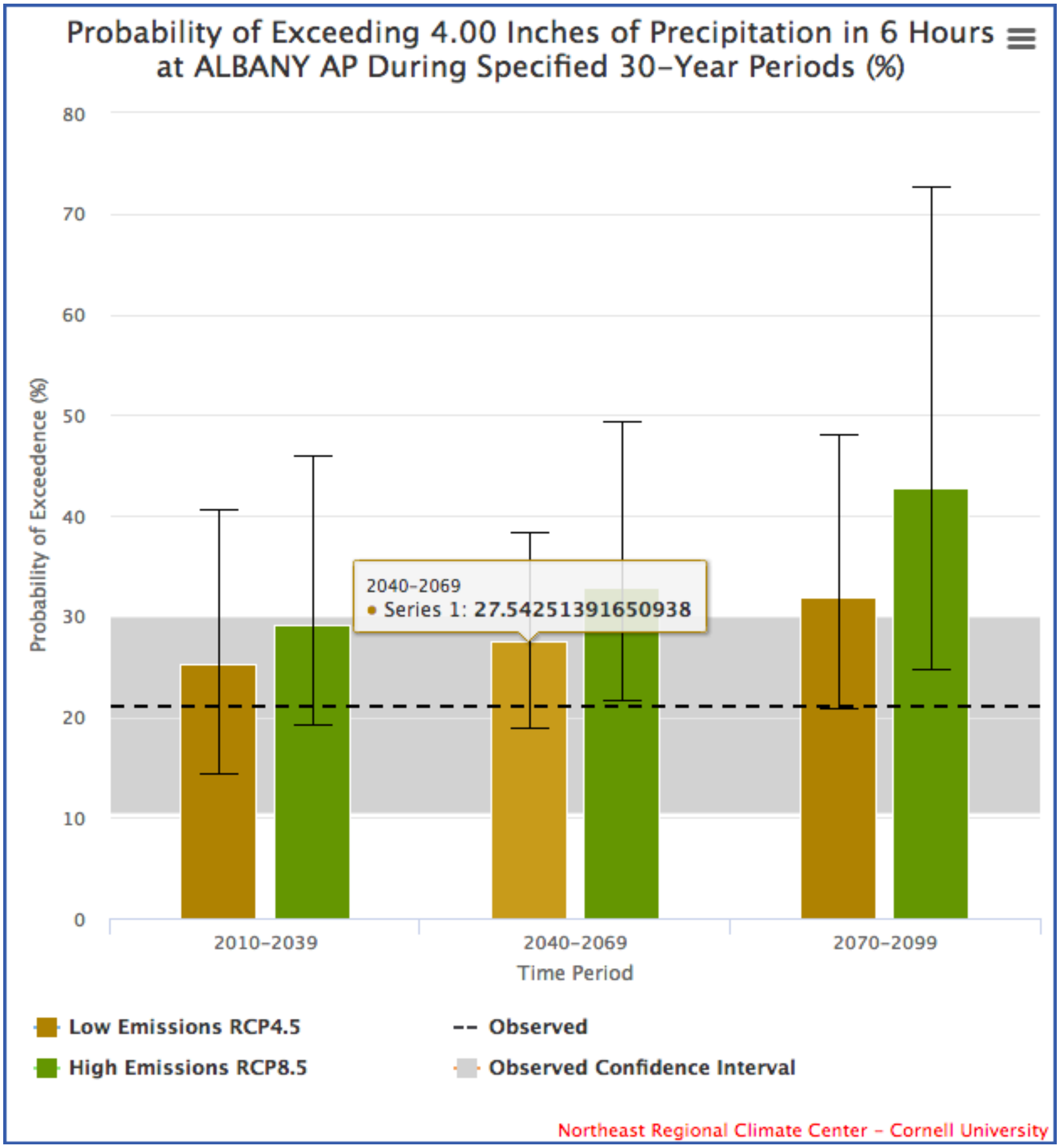

Figure 16: Bar plots showing the historical and future probability of 6-hour precipitation exceeding 4 inches at least once during a 30-year period at Albany, NY. The gray shaded region denotes the 90% confidence interval for the historical probability. The black error bars denote the range in future probabilities between the 10th percentile and 90th percentile downscaled projections.

Summary

This project employs three different methods to spatially downscale climate model output and create future projections of extreme precipitation throughout New York State. Future changes in extreme precipitation will likely have profound implications for various aspects of society, including public infrastructure, agriculture, and human health. In order to mitigate the potential consequences of such changes, it is imperative that we improve our understanding of how the frequency and magnitude of extreme precipitation are expected to change, and implement meaningful strategies that will allow society to adapt accordingly. Conclusions from this project will ultimately assist local and statewide decision-making with regard to climate change adaptation planning in New York State.

Acknowledgements

This research was supported by the New York State Energy Research and Development Authority (Contract 28257), with partial support from NOAA Contract EA133E07CN0090, the New York State Agricultural Experiment Station.

References

Allen, R. J., and A. T. DeGaetano, 2005: Areal reduction factors for two eastern United States regions with high rain-gauge density. *J. Hydrologic Engrg.,* **10,** 327–335.

Benestad, R. E., 2010: Downscaling precipitation extremes: Correction of analog models through PDF predictions. *Theor. Appl. Climatol.,* **100,** 1–21.

DeGaetano, A. T., 1998: A Smirnov test-based clustering algorithm with application to extreme precipitation data. *Water Resources Research,* **34,** 169–176.

DeGaetano, A. T., 2009: Time-dependent changes in extreme-precipitation return-period amounts in the continental United States. *J. Appl. Meteor. Climatol.,* **48,** 2086–2099.

Eden, J. M., and M. Widmann, 2014: Downscaling of GCM-simulated precipitation using model output statistics. *J. Climate,* **27,** 312–324.

Gao, X., C. A. Schlosser, P. Xie, E. Monier, and D. Entekhabi, 2014: An analogue approach to identify heavy precipitation events: Evaluation and application to CMIP5 climate models in the United States. *J. Climate,* **27,** 5941–5963.

Heideman, K. F., and J. M. Fritsch, 1988: Forcing mechanisms and other characteristics of significant summertime precipitation. *Wea. Forecasting,* **3,** 115–130.

Heineman, M., 2012: Trends in precipitation maxima at U.S. Historical Climatology Network stations 1893–2010. *World Environmental and Water Resources Congress 2012*.

Hosking, J. R. M., and J. R. Wallis, 1997: *Regional Frequency Analysis: An Approach Based on L-moments.* Cambridge University Press, 244 pp.

IPCC, 2014: Summary for policymakers. In: *Climate Change 2014: Impacts, Adaptation, and Vulnerability. Part A: Global and Sectoral Aspects. Contribution of Working Group II to the Fifth Assessment Report of the Intergovernmental Panel on Climate Change* [Field, C. B., V. R. Barros, D. J. Dokken, K. J. Mach, M. D. Mastrandrea, T. E. Bilir, M. C 683 hatterjee, K. L. Ebi, Y. O. Estrada, R. C. Genova, B. Girma, E. S. Kissel, A. N. Levy, S. MacCracken, P. R. Mastrandrea, and L. L. White (eds.)]. Cambridge University Press, Cambridge, United Kingdom and New York, NY, USA, 32 pp.

Jones, C., F. Giorgi, and G. Asrar, 2011: The Coordinated Regional Downscaling Experiment: CORDEX; an international downscaling link to CMIP5. *CLIVAR Exch.,* **16,** 34–40.

Kalnay, E., and Coauthors, 1996: The NCEP/NCAR 40-year reanalysis project. *Bull. Amer. Meteor. Soc.,* **77,** 437–471.

Karl, T. R., J. M. Melillo, and T. C. Peterson, 2009: *Global Climate Change Impacts in the United States* [Karl, T. R., J. M. Melillo, and T. C. Peterson (eds.)]. Cambridge

University Press, Cambridge, United Kingdom and New York, NY, USA, 189 pp.

Konrad, C. E., 1997: Synoptic-scale features associated with warm season heavy rainfall over the interior southeastern United States. *Wea. Forecasting,* **12,** 557–571.

Kunkel, K. E., K. Andsager, and D. R. Easterling, 1999: Long-term trends in extreme precipitation events over the conterminous United States and Canada. *J. Climate,* **12,** 2515–2527.

Kunkel, K. E., 2003: North American trends in extreme precipitation. *Nat. Hazards,* **29,** 291–305.

Kunkel, K. E., D. R. Easterling, D. A. R. Kristovich, B. Gleason, L. Stoecker, and R. Smith, 2012: Meteorological causes of the secular variations in observed extreme precipitation events for the conterminous United States. *J. Hydrometeor.,* **13,** 1131–1141.

Kunkel, K. E., L. E. Stevens, S. E. Stevens, L. Sun, E. Janssen, D. Wuebbles, and J. G. Dobson, 2013: Regional Trends and Scenarios for the U.S. National Climate Assessment: Part 9. Climate of the Contiguous United States. NOAA Technical Report NESDIS 142-9. Prepared by the National Oceanic and Atmospheric Administration, National Environmental Satellite, Data, and Information Service, Washington, D.C., 85 pp.

Maddox, R. A., C. F. Chappell, and L. R. Hoxit, 1979: Synoptic and meso-α scale aspects of flash flood events. *Bull. Amer. Meteor. Soc.,* **60,** 115–123.

McKay, M., and D. S. Wilks, 1995: Atlas of short-duration precipitation extremes for the northeastern United States and southeastern Canada. Northeast Regional Climate Center Research Publication RR 95-1, 26 pp.

Mielke, P. W., and E. S. Johnson, 1974: Some generalized beta distributions of the second kind having desirable application features in hydrology and meteorology. *Water Resources Research,* **10,** 223–226.

Panofsky, H. W., and G. W. Brier, 1968: *Some Applications of Statistics to Meteorology*. The Pennsylvania State University Press, 224 pp.

Perica, S., D. Martin, S. Pavlovic, I. Roy, M. St. Laurent, C. Trypaluk, D. Unruh, M. Yekta, and G. Bonnin, 2013: NOAA Atlas 14: Precipitation-Frequency Atlas of the United States, Vol. 9. Prepared by the U.S. Department of Commerce, National Oceanic and Atmospheric Administration, National Weather Service, Silver Spring, MD, 43 pp.

Press, W. H., B. P. Flannery, S. A. Teukolsky, and W. T. Vettering, 1986: *Numerical Recipes: The Art of Scientific Computing*. Cambridge University Press, 818 p.

Taylor, K. E., R. J. Stouffer, and G. A. Meehl, 2012: An overview of CMIP5 and the experiment design. *Bull. Amer. Meteor. Soc.,* **93,** 485–498.

Ward, J. H., 1963: Hierarchical grouping to optimize an objective function. *J. Amer. Statist. Assoc.,* **58,** 236–244.

Wilby, R. L., and T. M. L. Wigley, 1997: Downscaling general circulation model output: a review of methods and limitations. *Progress in Physical Geography,* **21,** 530–548.

Wilby, R. L., S. P. Charles, E. Zorita, B. Timbal, P. Whetton, and L. O. Mearns, 2004: Guidelines for use of climate scenarios developed from statistical downscaling methods. Prepared by the Intergovernmental Panel on Climate Change, Task Group on Scenarios for Climate Impact Assessment, Geneva, Switzerland, 27 pp.

Wilks, D. S., 1993: Comparison of 3-parameter probability distributions for representing annual extreme and partial-duration precipitation series. *Water Resour. Res.,* **29,** 3543–3549.

Wilks, D. S., and R. P. Cember, 1993: Atlas of Precipitation Extremes for the Northeastern United States and Southeastern Canada. Northeast Regional Climate Center Research Publication RR 93-5, 40 pp.

Winkler, J. A., 1988: Characteristics of summertime extreme rainstorms in Minnesota. *Ann. Assoc. Amer. Geogr.,* **78,** 57–73.

Appendix A: List of Stations

Station ID	Country	State	Station Name	Lat (°N)	Lon (°E)	Elev (ft)
060806	US	CT	BRIDGEPORT SIKORSKY MEM AP	41.16	−73.13	5
061762	US	CT	DANBURY	41.40	−73.42	405
062658	US	CT	FALLS VILLAGE	41.95	−73.37	550
063207	US	CT	GROTON	41.35	−72.04	40
065445	US	CT	NORFOLK 2 SW	41.97	−73.22	1340
066966	US	CT	ROCKY RIVER DAM	41.58	−73.43	220
067373	US	CT	SHEPAUG DAM	41.72	−73.30	840
199371	US	MA	WEST OTIS	42.18	−73.22	1295
281327	US	NJ	CANISTEAR RSVR	41.11	−74.48	1100
281335	US	NJ	CANOE BROOK	40.74	−74.35	180
281582	US	NJ	CHARLOTTEBURG RSVR	41.03	−74.42	760
283516	US	NJ	GREENWOOD LAKE	41.14	−74.32	470
286026	US	NJ	NEWARK INTL AP	40.68	−74.17	7
286146	US	NJ	NEW MILFORD	40.96	−74.02	12
286460	US	NJ	OAK RIDGE RSVR	41.00	−74.50	880
287079	US	NJ	PLAINFIELD	40.60	−74.40	90
287587	US	NJ	RINGWOOD	41.09	−74.27	305
288644	US	NJ	SUSSEX 2 NW	41.22	−74.66	649
289832	US	NJ	WOODCLIFF LAKE	41.01	−74.04	103
300042	US	NY	ALBANY AP	42.74	−73.81	312
300055	US	NY	ALBION 2 NE	43.27	−78.17	440
300063	US	NY	ALCOVE DAM	42.47	−73.93	607
300085	US	NY	ALFRED	42.25	−77.76	1706
300093	US	NY	ALLEGANY SP	42.10	−78.75	1500
300183	US	NY	ANGELICA	42.30	−78.02	1483
300331	US	NY	AURORA RSCH FARM	42.73	−76.66	830
300343	US	NY	AVON	42.92	−77.76	545
300443	US	NY	BATAVIA	43.03	−78.17	913
300448	US	NY	BATH	42.35	−77.35	1120
300608	US	NY	BENNETTS BRG	43.53	−75.95	660
300668	US	NY	BIG MOOSE 3 SE	43.80	−74.87	1760
300687	US	NY	BINGHAMTON GREATER AP	42.21	−75.98	1595
300785	US	NY	BOONVILLE 4 SSW	43.44	−75.37	1550
300889	US	NY	BRIDGEHAMPTON	40.95	−72.31	60
301012	US	NY	BUFFALO NIAGARA INTL AP	42.94	−78.74	705
301152	US	NY	CANANDAIGUA 3 S	42.85	−77.28	720
301168	US	NY	CANDOR 2 SE	42.19	−76.31	920
301185	US	NY	CANTON 4 SE	44.58	−75.11	448
301401	US	NY	CHAZY	44.88	−73.40	157
301413	US	NY	CHEMUNG	42.00	−76.64	822
301424	US	NY	CHEPACHET	42.91	−75.11	1320
301492	US	NY	CINCINNATUS	42.54	−75.89	1050
301623	US	NY	COLDEN 1 N	42.66	−78.68	1025
301752	US	NY	COOPERSTOWN	42.72	−74.93	1257

301966	US	NY	DANNEMORA	44.72	−73.72	1340
301974	US	NY	DANSVILLE	42.57	−77.72	660
302036	US	NY	DELHI 2 SE	42.26	−74.91	1420
302060	US	NY	DEPOSIT	42.06	−75.43	1000
302129	US	NY	DOBBS FERRY ARDSLEY	41.01	−73.83	200
302554	US	NY	ELIZABETHTOWN	44.21	−73.60	611
302574	US	NY	ELLENBURG DEPOT	44.91	−73.82	950
302610	US	NY	ELMIRA	42.10	−76.84	947
303025	US	NY	FRANKLINVILLE	42.33	−78.46	1590
303033	US	NY	FREDONIA	42.45	−79.31	760
303284	US	NY	GLENS FALLS FARM	43.33	−73.73	504
303294	US	NY	GLENS FALLS AP	43.35	−73.62	321
303346	US	NY	GOUVERNEUR 3 NW	44.35	−75.51	420
303773	US	NY	HEMLOCK	42.77	−77.61	902
303851	US	NY	HIGHMARKET	43.58	−75.52	1763
303983	US	NY	HORNELL ALMOND DAM	42.35	−77.70	1325
304025	US	NY	HUDSON CORRECTIONAL	42.25	−73.80	60
304102	US	NY	INDIAN LAKE 2 SW	43.76	−74.27	1660
304174	US	NY	ITHACA CORNELL UNIV	42.45	−76.45	960
304555	US	NY	LAKE PLACID 2 S	44.25	−73.98	1940
304731	US	NY	LIBERTY 1 NE	41.80	−74.74	1580
304772	US	NY	LINDLEY 2 N	42.06	−77.15	1040
304791	US	NY	LITTLE FALLS CITY RSVR	43.06	−74.87	893
304808	US	NY	LITTLE VALLEY	42.25	−78.81	1625
304836	US	NY	LOCKE 2 W	42.67	−76.47	1200
304912	US	NY	LOWVILLE	43.80	−75.48	860
305134	US	NY	MASSENA INTL AP	44.94	−74.85	214
305310	US	NY	MIDDLETOWN 2 NW	41.46	−74.45	700
305334	US	NY	MILLBROOK	41.86	−73.67	820
305377	US	NY	MINEOLA	40.73	−73.62	96
305426	US	NY	MOHONK LAKE	41.77	−74.16	1245
305512	US	NY	MORRISVILLE 6 SW	42.84	−75.73	1681
305714	US	NY	NEWCOMB	43.97	−74.22	1647
305751	US	NY	NEW LONDON LOCK 22	43.21	−75.65	400
305801	US	NY	NEW YORK CNTRL PK TWR	40.78	−73.97	130
305803	US	NY	NEW YORK JFK INTL AP	40.64	−73.76	11
305811	US	NY	NEW YORK LAGUARDIA AP	40.78	−73.88	11
305925	US	NY	NORTH CREEK 5 SE	43.66	−73.90	890
306062	US	NY	NORTHVILLE	43.16	−74.20	790
306085	US	NY	NORWICH	42.51	−75.52	989
306164	US	NY	OGDENSBURG 4 NE	44.73	−75.44	280
306196	US	NY	OLEAN	42.07	−78.45	1420
306314	US	NY	OSWEGO EAST	43.46	−76.49	350
306538	US	NY	PERU 2 WSW	44.57	−73.57	510
306623	US	NY	PISECO	43.46	−74.52	1730
306745	US	NY	PORTAGEVILLE	42.57	−78.04	1168
306774	US	NY	PORT JERVIS	41.38	−74.68	470

307134	US	NY	RIVERHEAD RSCH FARM	40.96	−72.72	100
307167	US	NY	ROCHESTER GTR INTL AP	43.12	−77.68	533
307205	US	NY	ROCK HILL 3 SW	41.59	−74.61	1270
307329	US	NY	RUSHFORD	42.39	−78.25	1540
307484	US	NY	SARATOGA SPRINGS 4 S	43.03	−73.82	310
307705	US	NY	SHERBURNE	42.68	−75.51	1095
307713	US	NY	SHERMAN	42.16	−79.59	1560
307780	US	NY	SKANEATELES	42.95	−76.43	875
307799	US	NY	SLIDE MTN	42.02	−74.42	2650
307842	US	NY	SODUS CTR	43.21	−77.01	420
308160	US	NY	STAMFORD	42.40	−74.63	1779
308383	US	NY	SYRACUSE HANCOCK INTL AP	43.11	−76.10	413
308578	US	NY	TRENTON FALLS	43.28	−75.16	800
308600	US	NY	TROY L&D	42.75	−73.68	24
308627	US	NY	TULLY HEIBERG FOREST	42.76	−76.08	1899
308631	US	NY	TUPPER LAKE SUNMOUNT	44.23	−74.44	1680
308944	US	NY	WANAKENA RNGR SCHOOL	44.15	−74.90	1510
308987	US	NY	WATERLOO	42.90	−76.86	452
309000	US	NY	WATERTOWN	43.98	−75.88	497
309005	US	NY	WATERTOWN INTL AP	43.99	−76.02	318
309072	US	NY	WELLSVILLE	42.12	−77.95	1510
309292	US	NY	WEST POINT	41.39	−73.96	320
309389	US	NY	WHITEHALL	43.56	−73.40	119
309405	US	NY	WESTCHESTER CO AP	41.07	−73.71	379
309425	US	NY	WHITESVILLE	42.04	−77.77	1740
309516	US	NY	WINDHAM 3 E	42.30	−74.20	1680
360868	US	PA	BRADFORD 4 SW RSCH 5	41.90	−78.71	1660
361832	US	PA	COVINGTON 2 WSW	41.73	−77.12	1745
362629	US	PA	EMPORIUM	41.51	−78.23	1040
362671	US	PA	EQUINUNK	41.87	−75.27	890
362682	US	PA	ERIE INTL AP	42.08	−80.18	730
363130	US	PA	GALETON	41.74	−77.65	1345
363311	US	PA	GLEN HAZEL 2 NE DAM	41.56	−78.60	1720
363758	US	PA	HAWLEY 1 E	41.48	−75.17	890
364432	US	PA	KANE 1 NNE	41.68	−78.80	1750
365606	US	PA	MEADVILLE 1 S	41.63	−80.17	1065
365915	US	PA	MONTROSE	41.85	−75.86	1420
367029	US	PA	PLEASANT MT 1 W	41.74	−75.45	1800
367103	US	PA	PORT ALLEGANY	41.82	−78.29	1475
368596	US	PA	STROUDSBURG	41.01	−75.19	460
368692	US	PA	SUSQUEHANNA	41.95	−75.60	910
368888	US	PA	TITUSVILLE WTR WORKS	41.63	−79.69	1220
368905	US	PA	TOWANDA 1 S	41.75	−76.44	760
368959	US	PA	TROY 1 NE	41.79	−76.77	1045
369042	US	PA	UNION CITY FILT PLT	41.90	−79.82	1400
369298	US	PA	WARREN	41.85	−79.15	1210
374266	US	RI	KINGSTON	41.49	−71.54	114

431081	US	VT	BURLINGTON INTL AP	44.47	−73.15	330
437098	US	VT	SALISBURY 2 N	43.93	−73.10	420
CA006100971	CA	ON	BROCKVILLE PCC	44.60	−75.67	314
CA006101874	CA	ON	CORNWALL	45.02	−74.75	209
CA006103367	CA	ON	HARTINGTON IHD	44.43	−76.70	524
CA006104175	CA	ON	KINGSTON PUMPING STATION	44.23	−76.48	252
CA006105460	CA	ON	MORRISBURG	44.92	−75.18	269
CA006105976	CA	ON	OTTAWA CDA	45.38	−75.72	259
CA006106000	CA	ON	OTTAWA INTL AIRPORT	45.32	−75.67	373
CA006139445	CA	ON	WELLAND	43.00	−79.27	574
CA006153194	CA	ON	HAMILTON AIRPORT &	43.17	−79.93	783
CA007023270	CA	QC	IBERVILLE	45.33	−73.25	101
CA007024100	CA	QC	LAPRAIRIE	45.38	−73.43	98
CA007025250	CA	QC	MONTREAL DORVAL INTL AP	45.47	−73.75	98
CA007025745	CA	QC	ORMSTOWN	45.12	−74.05	150
CA007026040	CA	QC	PHILIPSBURG	45.03	−73.08	173
CA007026836	CA	QC	ST ANICET 1	45.12	−74.28	154
CA007027040	CA	QC	STE CLOTILDE	45.17	−73.68	170
CA007028680	CA	QC	VALLEYFIELD	45.23	−74.10	150

Appendix B: List of CMIP5 Models

CMIP5 Model ID	Modeling Center/Group	Resolution
ACCESS1.0*	CSIRO, Australia	1.25° × 1.875°
ACCESS1.3*	CSIRO, Australia	1.25° × 1.875°
BCC−CSM1.1	Beijing Climate Center, China	1.125° × 1.125°
BCC−CSM1.1(m)	Beijing Climate Center, China	2.8° × 2.8°
BNU−ESM	Beijing Normal University, China	2.8° × 2.8°
CCSM4	National Centre for Atmospheric Research, USA	0.9° × 1.25°
CMCC−CM*	Euro−Mediterranean Centre on Climate Change, Italy	0.75° × 0.75°
CNRM−CM5	National Centre for Meteorological Research, France	1.4° × 1.4°
CSIRO−Mk3.6.0	CSIRO, Australia	1.875° × 1.875°
CanESM2	Canadian Centre for Climate Modeling and Analysis, Canada	1.875° × 1.875°
FGOALS−g2*	LASG, China	2.8° × 2.8°
GFDL−CM3	Geophysical Fluid Dynamics Laboratory, USA	2.0° × 2.5°
GFDL−ESM2G	Geophysical Fluid Dynamics Laboratory, USA	2.0° × 2.5°
GFDL−ESM2M	Geophysical Fluid Dynamics Laboratory, USA	2.0° × 2.5°
GISS−E2−H	NASA Goddard Institute for Space Sciences, USA	2.0° × 2.5°
GISS−E2−R	NASA Goddard Institute for Space Sciences, USA	2.0° × 2.5°
HADGEM2−ES*	Met Office Hadley Centre, United Kingdom	1.25° × 1.875°
IPSL−CM5A−LR	Pierre Simon Laplace Institute, France	1.9° × 3.75°
IPSL−CM5A−MR	Pierre Simon Laplace Institute, France	1.25° × 2.5°
IPSL−CM5B−LR	Pierre Simon Laplace Institute, France	1.9° × 3.75°
MIROC−ESM	JAMSTEC/AORI/NIES, Japan	2.8° × 2.8°
MIROC−ESM−CHEM	JAMSTEC/AORI/NIES, Japan	2.8° × 2.8°
MIROC5	JAMSTEC/AORI/NIES, Japan	1.4° × 1.4°
MRI−CGCM3	Meteorological Research Institute, Japan	1.125° × 1.125°
NorESM1−M	Norwegian Climate Center, Norway	1.9° × 2.5°

* These models were used for the delta method but not the analog method.